



HAL
open science

Terahertz Nondestructive Stratigraphic Analysis of Complex Layered Structures: Reconstruction Techniques

Min Zhai, D. Citrin, A. Locquet

► **To cite this version:**

Min Zhai, D. Citrin, A. Locquet. Terahertz Nondestructive Stratigraphic Analysis of Complex Layered Structures: Reconstruction Techniques. *Journal of Infrared, Millimeter and Terahertz Waves*, 2021, 10.1007/s10762-021-00819-1 . hal-03419745

HAL Id: hal-03419745

<https://hal.science/hal-03419745>

Submitted on 8 Nov 2021

HAL is a multi-disciplinary open access archive for the deposit and dissemination of scientific research documents, whether they are published or not. The documents may come from teaching and research institutions in France or abroad, or from public or private research centers.

L'archive ouverte pluridisciplinaire **HAL**, est destinée au dépôt et à la diffusion de documents scientifiques de niveau recherche, publiés ou non, émanant des établissements d'enseignement et de recherche français ou étrangers, des laboratoires publics ou privés.

Terahertz Nondestructive Stratigraphic Analysis of Complex Layered Structures: Reconstruction Techniques

Min Zhai,^{1,2} D.S. Citrin,^{1,2,✉} Alexandre Locquet,^{1,2}

1. Georgia Tech-CNRS IRL2958, Georgia Tech Lorraine, 2 Rue Marconi, 57070 Metz France
2. School of Electrical and Computer Engineering, Georgia Institute of Technology, Atlanta, GA 30332-0250 USA

✉Correspondence: david.citrin@ece.gatech.edu.

Abstract:

Terahertz (THz) time-of-flight tomography (TOFT), a nondestructive-evaluation technique for the stratigraphic characterization of structures with layers on the micron-to-millimeter scales, has proven to be challenging to apply to samples containing both micron-scale *and* millimeter-scale layers. In THz TOFT, echoes reflected from distant interfaces and defects are often obscured as they may be immersed in a noisy background as such features in the reflected signal may be weak due to attenuation and dispersion, leading to the loss of valuable information. Moreover, overlapping echoes from any optically thin layers, such as thin coatings on thick specimens, are likely to be mistaken for a single interface in reconstructing the stratigraphy. Thus, layered structures containing both thick and thin layers have proven problematic for THz TOFT characterization. In this paper, a sparse-deconvolution (SD) technique, based on an interior-point method, and including a propagation model accounting for dispersion is demonstrated. The method is shown to be successful in extracting the impulse response of samples that combine the challenges of both thick and thin layers. The robustness and effectiveness of this method are verified numerically and experimentally. While the SD approach does not perform quite as well as cross-correlation (CC) techniques in terms of maximum thickness, it can provide a clearer and more accurate reconstruction of moderately thick samples incorporating thin layers.

Keywords: Nondestructive testing; Terahertz imaging; Sparse deconvolution; Preconditioned conjugate gradient; Dispersion.

I. Introduction:

Nondestructive-evaluation (NDE) techniques are in demand across a range of industries for monitoring product quality and structure. Terahertz (THz) electromagnetic probes are attractive for electrically insulating materials due to their nondestructive, non-ionizing, and contactless nature also providing information down to the micron scale with conventional resolution limits down to tens of microns. The frequency range of THz electromagnetic waves—conventionally 100 GHz to 10 THz—lies at the border between microwaves and the infrared; in some cases, THz waves penetrate deeper than infrared light and may provide structural information about materials and components that may offer little x-ray contrast. Moreover, as non-ionizing radiation, in contrast to ultraviolet light and x-rays, THz waves at the relevant powers present no known health risks to biological tissue. Due to these advantages, THz-based techniques have achieved success in a variety of fields, such as heritage science [1-5], steel industry [6-9], as

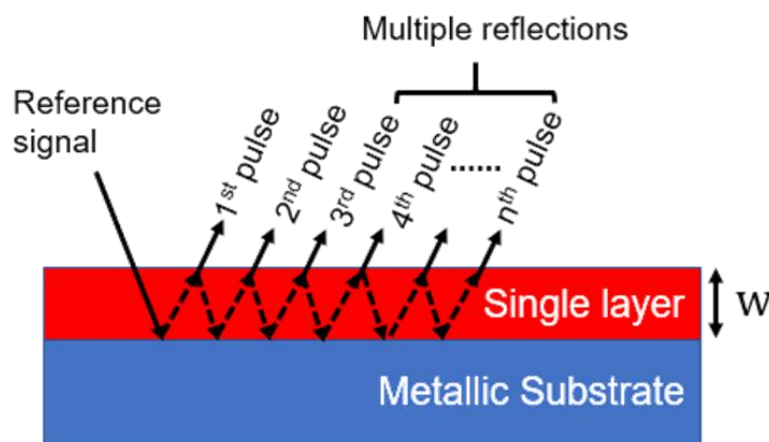


Fig. 1. Schematic diagram of THz TOFT.

well as biomedical applications [10-11].

One such technique to acquire qualitative and quantitative information concerning the internal layer structure, or *stratigraphy*, of optically opaque, electrically insulating objects is THz time-of-flight tomography (TOFT). In principle, after the generation of a quasi-single-cycle THz pulse typically based on nonlinear-optical interactions or photoconductive conversion of femtosecond near-infrared laser pulses, due to dielectric discontinuities in depth, the reflected THz pulses—or *echoes*—associated with the Fresnel coefficients between various interfaces are recorded as a function of transverse position in amplitude and time delay. The thickness of an individual layer can be estimated based on the optical delay between successive echoes and the dielectric properties of the corresponding layer within the THz range. A schematic diagram is shown in Fig. 1.

Visual examination of raw THz TOFT data is often inadequate to reconstruct the stratigraphy. Figure 1 shows a simple example of a THz TOFT experiment on a transmissive layer on top of a reflective metal in this example. Depending on the thickness w of the layer, however, there are two problematic situations to consider that place often conflicting demands on the reconstruction algorithm. When w is optically thin in THz regime (physical thickness divided by the refractive index n is less than about half the minimum wavelength within the usable bandwidth of the incident THz pulses), the reflected THz echoes from the front and back surfaces will strongly overlap, and thus visually distinct echoes from the two surfaces are not

observed. When, however, w is sufficiently large, the echo from the back surface may be close to or immersed within the noise floor due to attenuation and/or dispersion (pulse spreading/amplitude reduction). Clearly, a reconstruction technique that simultaneously has axial super-resolution capability, large dynamic range, and that can account in a straightforward fashion for dispersion is demanded.

Let us consider how these conflicting demands have been met. For the former case of optically thin layers, vast effort has been exerted to separate overlapping echoes, such as frequency wavelet-domain deconvolution (FWDD) [1,6,12], sparse deconvolution (SD) based on iterative shrinkage/thresholding (SD/IST) algorithm [2,13,14], autoregressive spectral extrapolation [8,15,16], numerical fitting combined with a rigorous one-dimensional electromagnetic model [17], advanced regression with a self-calibration model [18], and Hilbert transform together with multiple-signal spectrum estimation [19]. The second case, *viz.* a thick layer, however, has attracted only limited attention. In this case, we are not faced with the issue of temporally overlapping echoes; however, absorption and dispersion in the thick sample attenuates and distorts the echo coming from the back surface making it difficult to resolve. In reference [20], we proposed a cross-correlation (CC) approach (essentially a matched-filter-inspired approach) in conjunction with a quasi-Dirac δ -function dispersion model in THz TOFT thickness measurement of polycarbonate (PC) and polymethyl methacrylate (PMMA) plastic sheets in the few-mm range. Indeed, we found that such an approach theoretically enables us to measure sheets twice as thick as would be possible exploiting more naïve approaches.

Although the aforementioned CC-based method used in [20] succeeds in characterizing thick PC and PMMA plastic sheets, there are still some points that deserve to be mentioned: (1) Due to the dispersion as well as attenuation as a THz signal propagates through the material, echoes following the main pulse associated with the front air/plastic interface are reduced in amplitude and may have a low signal-to-noise ratio (SNR) for thick objects; therefore, errors may be introduced when estimating the pulse amplitude as well as the width. (2) In order to overcome the effect of noise, the calibration set must be large enough to upgrade the prediction accuracy of the quasi-Dirac δ -function model utilized to simulate dispersion. (3) The dispersion model and CC-based approach fail when echoes overlap partially or entirely. (4) Even though the CC-based approach is a robust tool that is less sensitive to background fluctuations, the obtained results are not suitable for *direct* post signal-processing due to the residual noise, in particular when the SNR of the reflected THz signal is not high enough. In the following, we propose an approach to tackle these shortcomings.

In this paper, we address how THz TOFT data can be used to reconstruct the stratigraphy of complex structures possessing both optically thin and thick layers. We employ an interior-point method, which is one type of second-order SD approach, to sparsely reconstruct the impulse response function of specimens which contain both optically thick and thin layers. The performance of the method is compared with two common THz signal-processing techniques, FWDD and CC. The preconditioned conjugate-gradient (PCG) algorithm is incorporated with the interior-point method to compute the search step for reducing the computational cost at each iteration. To balance pulse spreading, a dispersive propagation model is also utilized. The analysis enables the successful identification of various layer thicknesses. For example, in this study, we focus on a several-mm thick plastic sheet (for which dispersion plays a major rôle) with optically thin airgaps on the side of incidence and the opposite side created by a sheet of paper with a thin spacer on both sides of the plastic sheet. While the maximum determinable thickness by THz TOFT is less than that with SD compared with CC, SD with the interior-point

method can provide a more reliable and clearer signal reconstruction of a complex sample even in the absence of structural information of the materials.

In the following, we present the principles and implementation of the approach in Sec. II; in Sec. III, we present results and a discussion based on a case study of thick PMMA sheets with optical thin copy paper layer and air gap on both sides. We conclude in Sec. IV.

II. Principle:

In the time domain, the measured THz reflected signal $r(t)$ can be expressed as a convolution of the incident signal $i(t)$ and the impulse-response function $h(t)$ associated with the structure and properties of the measured sample, plus noise $n(t)$ originating in the THz generation, the environment, and the detection,

$$r(t) = i(t) \otimes h(t) + n(t). \quad (1)$$

The simplest approach of distinguishing signals reflected from samples embedded in noise is CC, which is expressed as [20]

$$\omega(t) = r(t) \otimes h(t) = \int_{-\infty}^{\infty} r(t) h(t + \tau) d\tau. \quad (2)$$

Even though the SNR of $\omega(t)$ is enhanced compared with $r(t)$ by reducing the noise's spectral bandwidth, CC fails to separate two overlapping signals reflected from an optical thin layer. Therefore, inaccurate reconstruction of the sample might result, especially in the absence of prior information about the structure (such as number of layers).

The other technique we frequently use to retrieve $h(t)$ is called FWDD, which first applies a bandpass filter $F(f)$ to eliminate anomalous spikes that might otherwise appear in the high-frequency region of the transfer function after the direct division between the Fourier transforms of $r(t)$ and $i(t)$,

$$h'(t) = IFFT(F(v) * \frac{FFT(r(t))}{FFT(h(t))}) \quad (3)$$

where FFT and $IFFT$ denote the Fourier transform and the inverse Fourier transform, respectively. Wavelet denoising is employed next further to improve the SNR of $h'(t)$, and the criterion of selecting an appropriate wavelet basis is determined by the similarity of mother wavelets and $i(t)$ **Error! Reference source not found.** Based on the nature of FWDD, it strongly relies on the waveform of $i(t)$ and fails to address the dispersion effect [19]. Thus, in some practical situations, its performance is quite limited.

Mathematically, the convolution model of the reflected THz signal $r(t)$ can be expressed as a matrix multiplication and formulated as

$$\mathbf{r} = \mathbf{I}\mathbf{h} + \mathbf{n} \quad (4)$$

\mathbf{I} is the convolution Toeplitz matrix whose rows are delayed version of the discretized incident signal, \mathbf{r} and \mathbf{h} are the vectors of THz reflected signal $r(t)$, impulse-response function $h(t)$, and noise $n(t)$, respectively; \mathbf{n} accounts for noise originating in the THz generation, the environment, and the detection.

One long-standing approach for problem (1) is the classical least-squares method, expressed as

$$\min_{\mathbf{x}} \frac{1}{2} \|\mathbf{I}\mathbf{h} - \mathbf{r}\|_2^2. \quad (5)$$

where $\|\cdot\|_2$ stands for the l_2 -norm. In practice, the least-square solution ignores the ill-posed

character of the deconvolution problems, and requires numerous iterations to recover \mathbf{h} ; therefore, regularization methods are required to stabilize the least-square solution.

One popular regularization technique, the l_1 -norm regularized optimization, is employed to force the retrieval of a sparse vector \mathbf{h} , and expressed as

$$\mathbf{min}_x \frac{1}{2} \|\mathbf{I}\mathbf{h} - \mathbf{r}\|_2^2 + \lambda \|\mathbf{h}\|_1 \quad (6)$$

where $\|\mathbf{h}\|_1 = \sum_m |\mathbf{h}_m|$, which stands for the sum of the absolute value of \mathbf{h} . The regularization parameter λ controls the trade-off between sparsity and reconstruction fidelity. The most impressive advantages of l_1 -norm regularized optimization over the l_0 - and l_2 - norm regularized optimization, are that it is not NP-hard [21], and can achieve sparse solution of Eq. (3). To date, this SD-based approach has been applied to process seismic and ultrasonic signals, speech recognition, and image reconstruction.

One of the standard algorithms for solving l_1 -norm regularized optimization is the iterative shrinkage algorithm (IST), which involves a matrix multiplication of \mathbf{I}^T and \mathbf{I} and a shrink/soft threshold operation in each iteration, and is given by

$$\mathbf{h}_{k+1} = \Psi_{\tau\phi} \left(\mathbf{h}_k - \tau \mathbf{I}^T (\mathbf{I}\mathbf{h}_k - \mathbf{r}) \right) \quad (7)$$

where τ is the step size and the soft-threshold operator $\Psi_{\tau\phi}(y) = \text{soft}(y, \tau)$, which is defined as $\text{soft}(y, \tau) = \text{sign}(y) \max\{|y| - \tau, 0\}$. Notice that $\mathbf{I}^T (\mathbf{I}\mathbf{h}_k - \mathbf{r})$ is the gradient of the data-fidelity term $\frac{1}{2} \|\mathbf{I}\mathbf{h} - \mathbf{r}\|_2^2$, demonstrating that each iteration takes a step τ along the direction given by the negative gradient of the data-fidelity term. Due to its simplicity and the low cost of each iteration, the first-order IST method is an attractive choice to address the l_1 -norm regularized least square problem. One typical example is that Dong *et al.* extracted the quantitative stratigraphy of a 17th century oil painting *Madonna in Preghiera* successfully using this approach [1].

Even though the SD/IST algorithm has been widely and straightforwardly implemented, many iterations are generally required to achieve high accuracy results, leading to large computation costs of SD/IST algorithm especially when addressing signals comprised of a large numbers of data points. A more detailed discussion can be found in Refs. [22,23].

Several refined approaches have been proposed to accelerate the IST algorithm, such as the fast IST algorithm (FISTA) [22], The two-step IST algorithm (TwIST) [24], and split augmented Lagrangian shrinkage algorithm (SALSA) [25]. In this project, an interior point method that utilizes PCG algorithm to compute the search direction, is utilized to solve l_1 -norm regularization. Compared with the SD/IST algorithm, super-linear convergence can be guaranteed and less iterations are demanded to achieve convergence, even though the computational cost of each iteration is significant. Therefore, a higher accuracy of the signal reconstruction can be achieved in some cases. Moreover, several approaches have been proposed to accelerate the PCG process, such as rank-one approximation of the matrix multiplication $\mathbf{I}^T \mathbf{I}$ [26]. Balancing the complexity with performance, an approximation of the Hessian matrix (which contains the matrix multiplication of $\mathbf{I}^T \mathbf{I}$) by its diagonal elements is employed in this work and presentation of the technique can be found in Ref. [27].

III. Results & Discussion:

Numerical simulation:

As mentioned above, we will show the effectiveness of SD for the characterization of a complex structure that contains both thick and thin layers. These two requirements place what appear to be conflicting demands on approaches employed in the literature to analyze THz TOFT data. To bring out the key issues, numerical simulations based on synthetic data (see schematic cross section in Fig. 1) are performed first to show the problems presented by typical approaches, such as the FWDD algorithm and the CC-based approach, and then to verify the potential advantages of SD for structural characterization on complex layered structures.

Considering the THz TOFT experiment as a linear time-invariant system, the reflected signal $r(t)$ is thus the convolution of the known THz pulse $i(t)$ (reference signal) [we use a typical experimentally measured reference signal, see inset in Fig. 2] and the impulse-response function $h(t)$. An ideal impulse response function $h_0(t)$ of a simple three-layer structure, represented in Fig. 2, is assumed,

$$h_0(t) = \begin{cases} 0.3 & t = 11.6 \\ 0.2 & t = 11.89 \\ -0.02 & t = 34.8 \\ -0.1 & t = 40.89 \\ -0.05 & t = 41.47 \\ 0 & \text{otherwise} \end{cases} \quad (8).$$

where the time t is in picoseconds; time-domain signals are discretized with the sampling period $T_s = 0.0116$ ps utilized later in experiments ($t = nT_s$ with n the discrete index). Nonzero values at a given time are related to the Fresnel coefficient from a given interface and determine the amplitude of the respective echoes. The time intervals (optical delays) between the 1st echo

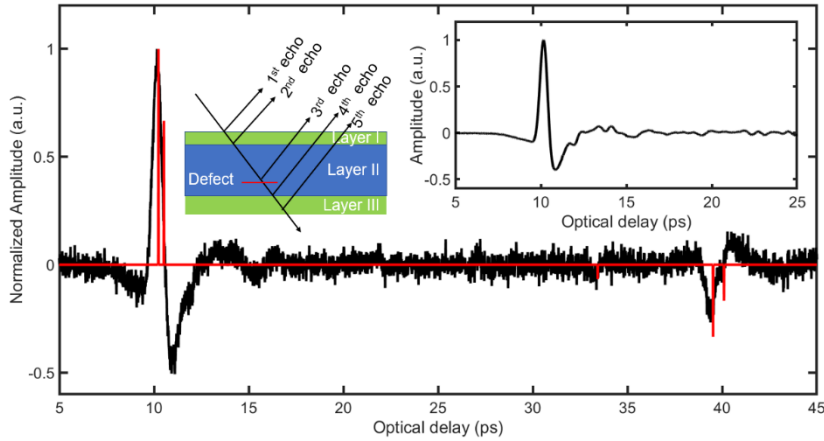


Fig. 2. The assumed impulse response function $h_0(t)$ (red) and the simulated reflected THz signal $r(t)$ (black). Inset shows an experimentally measured reference pulse $i(t)$ produced by our apparatus. Also shown is a schematic cross section of the simulated three-layered sample. The layers I and III (green) are Teflon of thicknesses 30 μm and 60 μm , respectively, while layer II (blue) is silica with thickness of ~ 2230 μm . A thin air layer exists around the central region of layer II.

and 2nd echo, 2nd echo and 4th echo, and 4th echo and 5th echo are 0.29 ps, 29 ps, and 0.58 ps, respectively, corresponding to the thickness of the layer I, II, and III. Assuming that the first and third layers are Teflon, and the second layer is amorphous silica, based on the corresponding averaged refractive index of Teflon and silica within the THz frequency regime, which are 1.45 [28] and 1.95 [29], respectively, the thicknesses of layers I, II, and III are 30 μm , 2230 μm , and 60 μm , respectively. In addition, a thin air layer is present in layer II at time

delay $t = 34.8$ ps. The discussion above holds in the absence of noise. In order to simulate the reflected signal $r(t)$ obtained in the actual noisy environment, additive Gaussian white noise with SNR 10 dB is included in the reflected signal $r(t)$ as shown in Fig. 2.

We expect five peaks (two positive peaks and three negative peaks) in $r(t)$. On account of the optical thin thicknesses of layers I and III, the echoes reflected from the front and back of these two layers almost entirely overlap. One may then erroneously conclude that the sample consists solely of a single layer. Furthermore, the amplitude of reflected echo from the small airgap is comparable to the noise background and difficult to be distinguished directly in the raw reflected signal $r(t)$. Further signal processing is thus necessary to obtain the thickness information of layers I, II, and III, as well as resolve the reflected echo from the small air layer that is drowned in noise.

Our first attempt is solely to apply a frequency-domain windowing filter, the conventional and simplest approach to denoise experimental signals. The frequency-domain filters must be used with caution, as meaningful information can be discarded along with the noise. In order to guarantee a satisfactory SNR of the deconvolved signal, the preferred approach is a time-localized filtering approach cascaded with mild filtering of the type above. Here we use wavelet denoising due to the high similarity between the wavelet basis functions and the typical THz signal [30]. How to select the optimal wavelet base function and to evaluate the decomposition level is discussed in detail in Refs. [31,32]. For this work, balancing the denoising performance of FWDD with the SNR of the simulated reflected signal $r(t)$, Wiener filtering with noise desensitizing factor $0.2 \max(|I(v)|^2)$, where $I(v)$ is the Fourier transform of the reference signal $i(t)$, is selected and the *sym4* wavelet function with decomposition level 10 are set for wavelet decomposition. We note that the performance of the Wiener filter is largely determined by the selection of noise desensitizing factor. Owing to the relatively low amplitude of the reflected

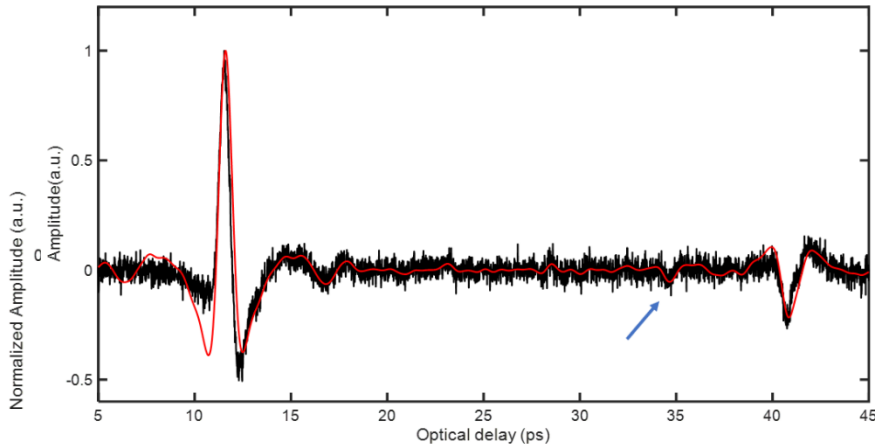


Fig. 4. Comparison between the raw reflected signal $r(t)$ (black) and the corresponding deconvolved result by CC (red) based on synthetic data. The arrow indicates the echo from the airgap at $t = 34.67$ ps. Results obtained with simulated data for the assumed impulse response function $h_0(t)$ of Eq. 5.

Fig. 3. Comparison between the raw reflected signal $r(t)$ (black) and the corresponding deconvolved signal by FWDD (red) based on the synthetic data. Results obtained with simulated data for the assumed impulse response function $h_0(t)$ of Eq. 5. Layer III is resolved successfully, while layer I and the air layer locations fail to be identified.

signal from the thin air layer within layer II, a larger noise desensitizing factor will lead to the elimination of the subtle features in the reflected signal $r(t)$.

The FWDD deconvolved signal for the synthetic reflected signal $r(t)$ is displayed in Fig. 3. Compared with the raw reflected signal $r(t)$ (black), the SNR of the deconvolved signal is

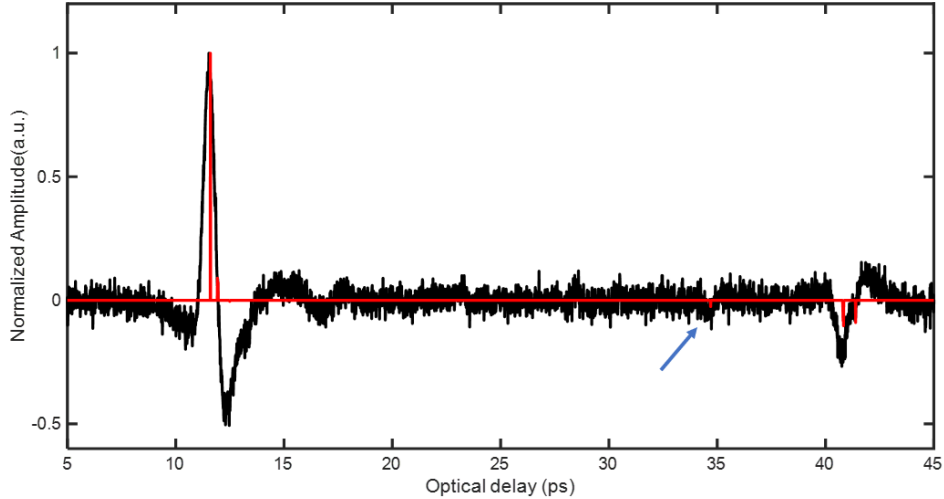


Fig. 5. Comparison between the raw reflected signal $r(t)$ (black) and the corresponding deconvolved result by SD (red) based on synthetic data. All interfaces are observed successfully in the deconvolved result. The blue arrow indicates the position of the echo from the airgap in layer II, which is identified in the SD reconstruction.

significantly enhanced. Owing to the presence of residual noise even after FWDD as well as to its relatively low amplitude of the signal, the echo corresponding to the thin air layer is difficult to be identified clearly in the deconvolved result. Importantly, the thin layer III is resolved successfully, while layer I fails to be resolved. Owing to the narrow effective bandwidth of the impulse response function $h(t)$, the axial resolution of FWDD is moderate. According to the numerical simulation presented in Ref. [15], the minimum time delay that is reconstructed by FWDD for our setup is ~ 0.35 ps when $\text{SNR} = 10$ dB, corresponding to a thickness for layers I and III of ~ 36 μm , which is larger than the assumed optical thicknesses for layers I and III in $h_0(t)$. Moreover, the appearance of extraneous peaks as well as the pulse broadening in the impulse response function recovered by FWDD, resulting from the application of the low-pass filter, are also observed in the deconvolved result, and might deteriorate the resolution in turn [19].

Because we have succeeded in identifying weak echoes from a noisy background using CC in Ref. [20], we next attempt that approach. Unlike FWDD that improves SNR mainly by narrowing the bandwidth of impulse response function $h(t)$, CC enhances SNR by reducing the noise's spectral bandwidth to that of the reference signal. Superior to FWDD, because of the absence of signal truncation, there is no risk of losing valuable information when applying CC. Therefore, in some cases, the results of CC may be more reliable than FWDD, in particular in the absence of prior knowledge of the structure and low SNR in the reflected signal $r(t)$. Figure 4 presents the comparison between $r(t)$ and $h(t)$ deconvolved by CC. The ability of CC to identify real echoes is higher than FWDD. The echo reflected from the thin air layer, as indicated by the blue arrow, is easily identified even with small amplitude, validating the superior capability of CC to pick out weak echoes in a low-SNR environment. Because CC is less sensitive to SNR, theoretically, it can even detect signals buried below the noise floor as opposed to FWDD. However, based on the nature of CC that extracts a known signal from a reflected signal contaminated by noise, it is not designed to separate overlapped echoes associated with optically thin layers. As a result of which, the echoes reflected from layers I and III cannot be distinguished. Due to these disadvantages, CC is not suitable for samples containing thin layers.

Having considered difficulties encountered in implementing FWDD and CC, we now

employ SD. In contrast to CC and FWDD, SD looks for a series of nonzero spikes (corresponding to echoes or reflections from material interfaces) in the reconstructed impulse-response function $h(t)$. That is, $h(t)$ is assumed to be sparse in the time domain, *i.e.*, zero almost everywhere. The approach proves convenient for subsequential signal processing, such as peak-detection, as discussed in Refs. [2,13]. SD can provide axial super-resolution while also performing well on thick layers, and is thus more suitable to investigate samples including thin layers or even in the absence of other information on the layer structure. Figure 5 is the reconstructed signal based on SD. Four nonzero peaks (two positive peaks and two negative peaks) associated with the interfaces of layers I, II, and III, and one weak peak reflected from

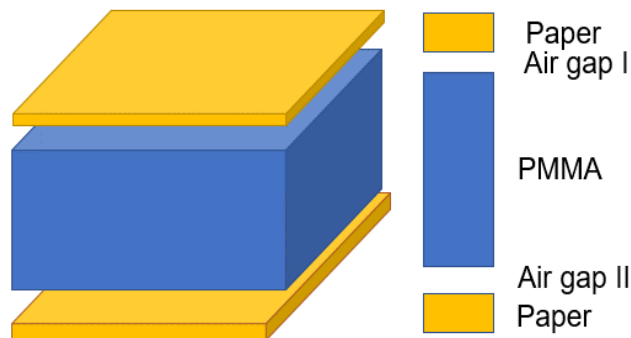


Fig. 6. Schematic diagram of experimentally measured samples, composed of two paper layers (yellow), two air gaps (white), and one thick PMMA plastic sheet (blue) in between. The papers are standard copy paper and the airgaps are produced by a suitable spacer layer. The thickness of PMMA ranges from 2 mm to 12 mm.

the thin air layer hidden in layer II, are found in the SD reconstructed impulse response function $h(t)$, confirming the higher resolution compared to FWDD and CC. The thickness of layers I, II, and III are calculated based on the corresponding optical distances Δt and listed in Table 1. The minimum thickness that can be resolved by SD, based on our numerical simulation, is $\sim 15 T_s$ with an SNR of 10 dB, corresponding to a Teflon layer with thickness of $18 \mu\text{m}$. Of note, the SD/IST algorithm, another type of SD our group has previously employed [2], has also been tested. Even though similar results are obtained, it involves a larger computational cost to achieve convergence and may not be well-suited for applications in which computational efficiency is required.

Table 1. Thickness comparison of layer I-III between SD results and nominal value.

| | LAYER I | LAYER II | LAYER III |
|---|-----------|-------------|-----------|
| Nominal thickness (μm) | 30 | ~ 2230 | 60 |
| SD results (μm) | ~ 33 | ~ 2224 | ~ 58 |

Experimental verification:

In the above numerical demonstration based on synthetic data, SD exhibited better performance in addressing a sample having both thick and thin layers. In this section, actual multi-layered structures are designed to evaluate the performance of SD experimentally. The experimental data is then analyzed based on FWDD, CC, and SD. A schematic diagram of the sample is shown in Fig. 6. It is a five-layer structure with a layer of standard copy paper on each side of a thick PMMA plastic sheet. Airgaps are introduced intentionally between standard copy paper and the PMMA with a spacer. The paper thickness is $\sim 90 \mu\text{m}$ measured with a high-resolution caliper. The thickness of airgap is roughly $150 \mu\text{m}$. Six solid PMMA plastic sheets of various thicknesses $w=2, 4, 6, 8, 10,$ and 12 mm are utilized. Relevant physical properties of the PMMA sheets can be found in Ref. [20]. In order to prevent scattering in nonspecular directions, the top and bottom surfaces of the PMMA are diamond polished and shaped after fabrication.

THz transmission measurements were employed first to characterize the optical constants of PMMA. THz transmission measurements were employed first to characterize the optical constants of PMMA. Based on linear fitting of $n(\nu)$ for a 2-mm-thick PMMA sheet, shown in Fig. 7(a), the refractive index of PMMA at 1 THz is ~ 1.62 , and a negative dispersion between 0.2 and 2 THz, *viz.* $dn/d\nu \approx -0.01 \text{ THz}^{-1}$, is found after linear fit. A good fit between the measured $n(\nu)$ and the linearly modeled $n(\nu)$, is found. Similar results are also found for PMMA sheets of other thicknesses, and not presented here. The observation of negative dispersion at low frequency and the corresponding refractive index of PMMA in a good agreement with Ref. [33]. The optical constants of copy paper between 0.2 and 2 THz is also measured and presented in Fig. 7(b). A relatively frequency-independent refractive index is found (albeit the paper is

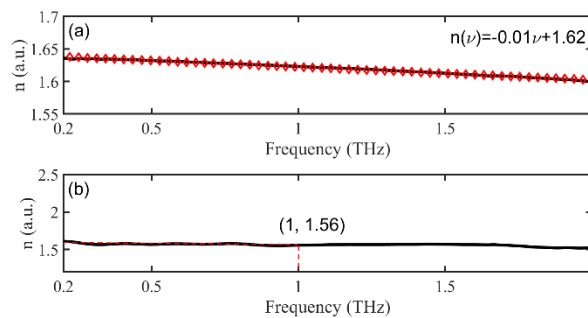


Fig. 7. (a). Comparison between $1.62-0.01\nu$ (red diamond line) with n measured in THz and the frequency-dependent refractive indices $n(\nu)$ (blue solid line) for PMMA. (b). the frequency-independent of refractive indices $n(\nu)$ for copy paper.

rather thin) with $n \sim 1.56$ at 1 THz.

After characterizing PMMA and copy paper in transmission measurements, THz TOFT experiments were carried out next for stratigraphic characterization of these samples. It is noted that the bandwidth of the setup (TeraView Ltd. THz-TDS Spectra 3000) extends to 3 THz, corresponding to wavelength $\sim 100 \mu\text{m}$; however, in practice, accounting for the SNR of the reflected signal, the usable bandwidth in $r(t)$ in these experiments is limited to about 2 THz. Any layer thickness $\lesssim 100 \mu\text{m}$ is thus considered optically thin. The spot size of the generated THz beam is frequency-dependent, and is about $300 \mu\text{m}$ at 1 THz and the depth of focus far

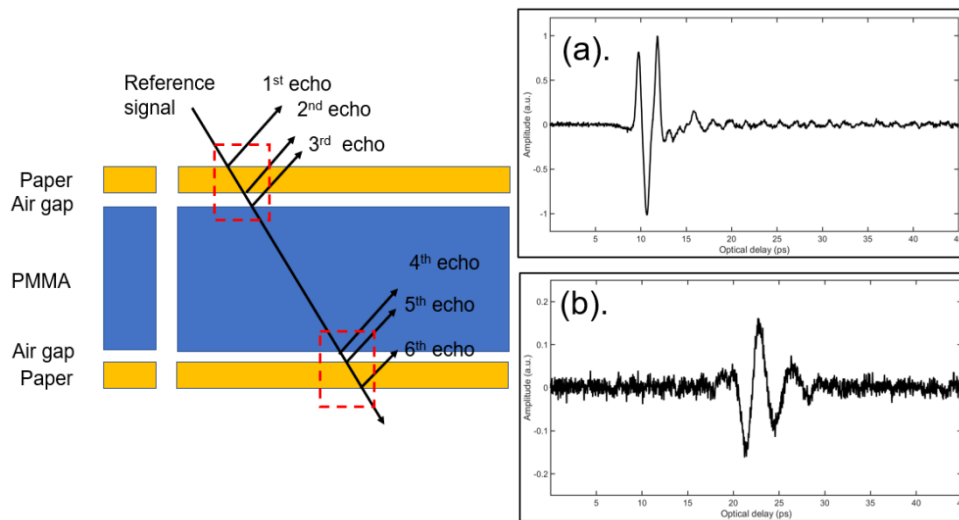


Fig. 8. Typical reflected temporal signal from the front and back of sample whose thickness of PMMA sheet is 6 mm. Notice the different vertical scales for (a) and (b).

exceeds the sample thickness, so that we can treat the beam as collimated in its interaction with the sample. A typical reflected temporal signal (normalized) from the front and back of the sample with 6-mm PMMA is shown in Fig. 8. Two positive and one negative echo are seen in Fig. 8(a). The first two positive echoes correspond to the air/ paper and airgap/PMMA interfaces. The sign of the second echo is negative due to the Fresnel coefficient from a high-to low- refractive index medium. However, when it comes to the signal reflected from the back of sample, the situation becomes complex owing to the low SNR ensuing attenuation during propagation. Moreover, even though dispersion in PMMA is weak in Fig. 7(a), the cumulative effect of the dispersion on $r(t)$ in thick samples could not be ignored. The reduction in the amplitudes of echoes following long-distance propagation inevitably contributes to the introduction of errors when seeking to locate the peak position as well as estimating the full width at half maximum (FWHM) of the echo.

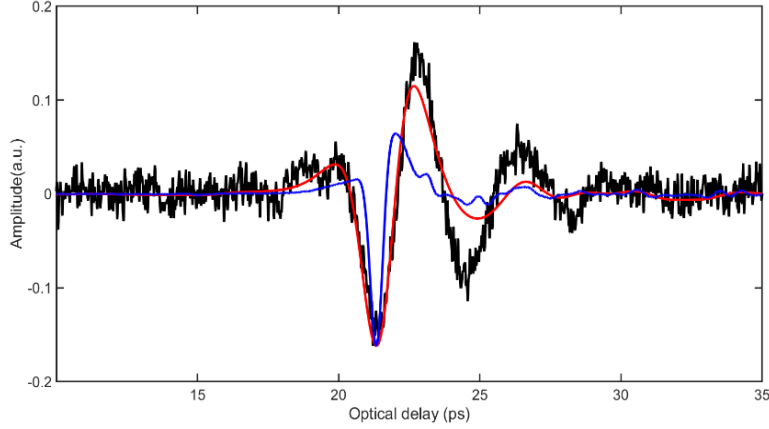


Fig. 9. Comparison of the raw reflected echoes from the back of the sample whose thickness of PMMA sheet is 6 mm (black), the reference signal (blue), and the signal propagated through back PMMA/airgap interface extrapolated based on the dispersion model (red).

According to our previous experience with synthetic data (see above), we directly employed SD to reconstruct $h(t)$. For thick PMMA, because of dispersion and attenuation, pulse-spreading and amplitude reduction occur in echoes associated with echoes that travel substantial distances in the sample, as shown in Fig. 9. Based on the nature of time-invariant systems, the reflected signal is the superposition of THz reference signals with suitable time-shifts and scaled amplitudes. The pulse broadening, if not taken into consideration, degrades the ability of the deconvolution techniques to reconstruct the stratigraphy. Specifically, to achieve an accurate structural representation of the back of sample, the transmitted signal through the back PMMA/airgap interface is used as the reference signal when investigating the echo reflected from the back of sample. This signal is estimated using the dispersive propagation model presented in Ref. [34]. Different from the quasi-Dirac δ -function dispersion model in Ref. [20] as well as the novel dispersion compensation strategy based on the double Gaussian mixture model (DGMM) in Ref. [35], because it does not involve a cumbersome parameter tuning process all relevant parameters are obtained from the transmission measurement, it is thus simpler and more straightforward to implement. High similarity between the extrapolated signal accounting for dispersion and the raw reflected signal at the back PMMA/air gap interface, is found and shown in Fig. 9.

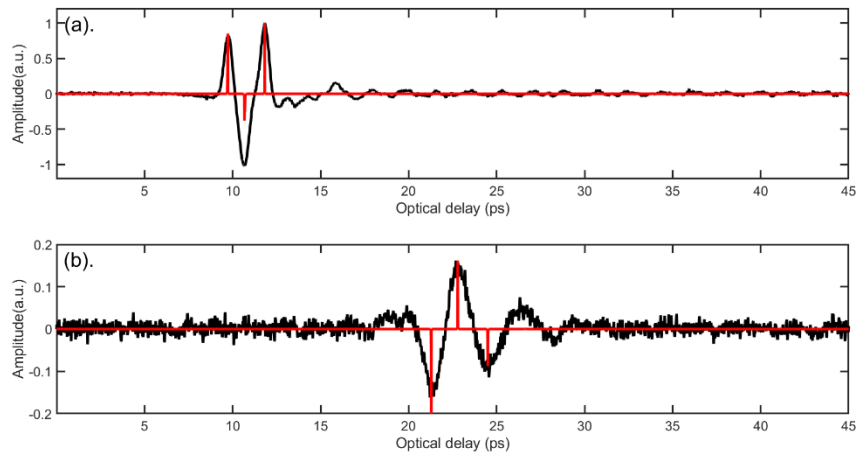


Fig. 10. The comparison between the deconvolved results by SD (red) and the raw reflected signal (black) from the front of sample (a), and the back of sample (b). The thickness of the PMMA sheet is 6 mm.

A deconvolved $h(t)$ only with several nonzero points to represent the structural features, is presented clearly in Fig. 10(a) and (b), and six sharp peaks, corresponding to echoes 1 through 6, are clearly observed. The thickness of the paper and airgap on both sides of the sample, as well as that of the thick PMMA plastic itself, can be estimated based on SD results. The

determined thicknesses are 87 μm , 167 μm , and 5.92 mm, respectively, showing excellent agreement with the independently measured values. It is also worth mentioning that dispersion is a crucial factor that cannot be ignored when analyzing the reflected signals from coatings on the back of the thick PMMA; if dispersion were neglected in the analysis, the broadened peak would be treated as the sum of several erroneous peaks by the algorithm of sparse deconvolution. Moreover, we find that when the thickness of PMMA larger than 8 mm, the 6th echo fails to be distinguished entirely.

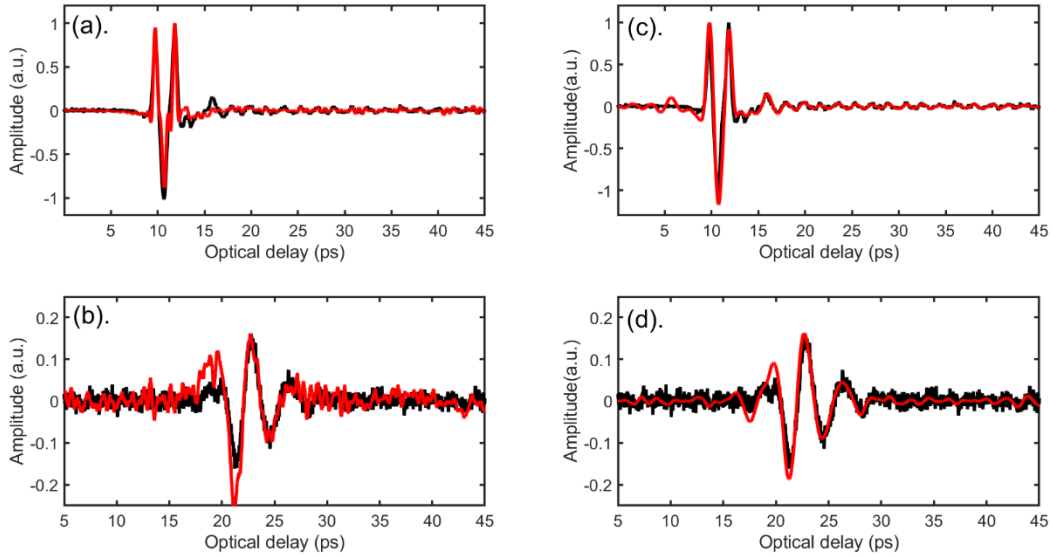


Fig. 11. Comparison between the deconvolved result (red) and the raw reflected signal (black) from the front of the sample by (a) FWDD and (c) CC. Comparison between the deconvolved result (red) and the raw reflected signal (black) from the back of sample by (b) FWDD and (d) CC. The thickness of the PMMA sheet is 6 mm.

The performance of FWDD and CC is also tested and the corresponding deconvolved results are presented in Fig. 11. Figures 11 (a) and (b) represent the reflected signals from the front and back of the PMMA sample when FWDD is employed. We observe some level of improvement in the SNR. In the case of the back reflections [Fig. 11(b)], however, the interpretation is arduous as the amplitudes of the postprocessed echoes are comparable to the noise floor and, further, side-peak oscillations are present. The deconvolved signal by FWDD are thus insufficient to provide a reliable reconstruction. Figures 11(c)-(d) show the signals reflected from the front and back of the PMMA sample when CC is employed. Pulse spreading is taken into consideration to overcome the severe waveform distortion of echoes from the back of sample. It is clear that the SNR of the reconstructed signal is greater than that yielded by FWDD and interface positions on the backside of the sample can be more easily identified. Interpretation is still not as clear as with the quasi-ideal impulse response provided by the SD technique; in particular, the width of the deconvolved echoes leads to estimation uncertainty and additional oscillations observed in the signal could be wrongly interpreted as interfaces. Even though CC performs well for thick samples on the ground that CC maximizes SNR when an *identical* waveform (echo) is immersed in noise, CC performs poorly and unreliable when thin layers are also involved.

The axial resolution of the SD algorithm also merits quantitative study. Considering the maximum dynamic range > 50 dB of the reference THz signal $h(t)$ generated by the experimental apparatus we observe through simulation that the maximum thickness w of PMMA plastic sheet that can be resolved by SD is ~ 17 mm, which is lower than the value for CC (~ 36 mm [19]). Even through the maximum resolvable thickness is lower than for CC, SD provides a clearer and more accurate assessment of the complex structure of samples with intermediate thickness and thin layers since CC fails to identify the thin layers. We last note

that multiple reflections are quite weak and have been ignored, even though for our axially symmetric structure, there are features arising from single echoes from the back surface and multiple echoes from the structure on the front surface that coincide with single echoes from the back surface. As the multiple echoes are quite weak, they do not significantly affect the analysis.

IV. Conclusion:

In this paper, SD based on an interior-point method in conjunction with a propagation model accounting for dispersion is demonstrated to be successful in reconstructing the stratigraphy of a complex sample incorporating both optically thick and thin layers. The use of an interior-point method with the preconditioned conjugate-gradient algorithm significantly decreases the computational cost of the SD technique compared to the standard iterative soft-thresholding algorithm. The dispersion model is used to take into account the significant attenuation and distortion endured by the THz signal in a thick sample. The proposed technique is compared to two other post-processing techniques, namely FWDD and CC. FWDD faces severe limitations as it is ill-suited to resolve thick samples [19] and can also fail to identify optically thin layers. CC has the advantage of performing well for thicker samples than SD, but is shown to fail to resolve additional thin layers in otherwise thick samples. We demonstrate that the inclusion of a dispersion model in the SD procedure increases the maximum sample thickness than can be resolved while maintaining a significantly better axial resolution than FWDD and CC. As illustrated by the experimental results, SD may be the preferred option for stratigraphic reconstruction of moderately thick samples with complex structure. For example, such an approach will be of value to characterize coatings on electrically insulating materials when there are constraints requiring access from the back side.

Acknowledgement:

We gratefully acknowledge the support of Conseil Régional Grand Est and CPER SusChemProc.

References:

- [1] J. Dong, J.B. Jackson, M. Melis, D. Giovanacci, G.C. Walker, A. Locquet, J.W. Bowen, and D.S. Citrin, "Terahertz frequency-wavelet domain deconvolution for stratigraphic and subsurface investigation of art painting," *Opt. Express*, vol. 24, no. 23, pp. 26972-26985, 2016.
- [2] J. Dong J, A. Locquet, M. Melis, and D.S. Citrin, "Global mapping of stratigraphy of an old-master painting using sparsity-based terahertz reflectometry," *Sci. Rep.*, vol. 7, no. 1, pp. 1-12, 2017.
- [3] C.L. Dandolo, J.P. Guillet, X. Ma, F. Fauquet, M. Roux, and P. Mounaix, "Terahertz frequency modulated continuous wave imaging advanced data processing for art painting analysis," *Opt. Express*, vol. 26, no. 5, pp. 5358-5367, 2018.
- [4] M. Mikerov, R. Shrestha, P. van Dommelen, D.M. Mittleman, and M. Koch, "Analysis of ancient ceramics using terahertz imaging and photogrammetry," *Opt. Express*, vol. 28, no. 15, pp. 22255-22263, 2020.
- [5] K. Krügener, J. Ornik, L.M. Schneider, A. Jäckel, C.L. Koch-Dandolo, E. Castro-Camus, N. Riedl-Siedow, M. Koch, and W. Viöl, "Terahertz inspection of buildings and architectural art," *Appl. Sci.*, vol. 10, no. 15, pp. 5166, 2020.
- [6] J. Dong, A. Locquet, and D.S. Citrin, "Terahertz quantitative nondestructive evaluation of failure modes in polymer-coated steel," *IEEE J Sel Top Quantum Electron.*, vol. 23, no. 4, pp. 1-7, 2016.
- [7] M. Zhai, A. Locquet, C. Roquelet, P. Alexandre, L. Dahéron, and D.S. Citrin, "Nondestructive measurement of mill-scale thickness on steel by terahertz time-of-flight tomography," *Surf. Coat. Technol.*, vol. 393, pp. 125765, 2020.
- [8] M. Zhai, A. Locquet, C. Roquelet, L.A. Ronqueti, and D.S. Citrin, "Thickness characterization of multi-layer coated steel by terahertz time-of-flight tomography," *NDT & E Int.*, vol. 116, pp. 102358, 2020.
- [9] F. Ellrich, M. Bauer, N. Schreiner, A. Keil, T. Pfeiffer, J. Klier, S. Weber, J. Jonuscheit, F. Friederich, and D. Molter, "Terahertz quality inspection for automotive and aviation industries," *J. Infrared Millim. Terahertz Waves*, vol. 41, no. 4, pp. 470-489, 2020.
- [10] J. Wang, Q. Sun, R.I. Stantchev, T.W. Chiu, A.T. Ahuja, and E. Pickwell-MacPherson, "In vivo terahertz imaging to evaluate scar treatment strategies: silicone gel sheeting," *Biomed. Opt. Express*, vol. 10, no. 7, pp. 3584-3590, 2019.
- [11] A. Gong, Y. Qiu, X. Chen, Z. Zhao, L. Xia, and Y. Shao, "Biomedical applications of terahertz technology," *Appl. Spectrosc. Rev.*, vol. 55, no. 5, pp. 418-438, 2020.
- [12] Y. Chen, S. Huang, and E. Pickwell-MacPherson, "Frequency-wavelet domain deconvolution for terahertz reflection imaging and spectroscopy," *Opt. Express*, vol. 18, no. 2, pp. 1177-1190, 2010.
- [13] J. Dong, X. Wu, A. Locquet, and D.S. Citrin, "Terahertz superresolution stratigraphic characterization of multilayered structures using sparse deconvolution," *IEEE Trans Terahertz Sci Technol.*, vol. 7, no. 3, pp. 260-267, 2017.
- [14] M. Zhai, A. Locquet, M. Jung, D. Woo, and D.S. Citrin, "Characterization of nanoporous Al₂O₃ films at terahertz frequencies," *Opt. Lett.*, vol. 45, no. 14, pp. 4092-4095, 2020.
- [15] J. Dong, A. Locquet, and D.S. Citrin, "Depth resolution enhancement of terahertz deconvolution by autoregressive spectral extrapolation," *Opt. Lett.*, vol. 42, no. 9, pp. 1828-1831, 2017.

- [16] M. Zhai, A. Locquet, C. Roquelet, and D.S. Citrin, "Terahertz Time-of-Flight Tomography Beyond the Axial Resolution Limit: Autoregressive Spectral Estimation Based on the Modified Covariance Method," *J. Infrared, Millim Terahertz Waves*, vol. 41, no. 8, pp. 926-939, 2020.
- [17] K. Su, Y.C. Shen, and J.A. Zeitler, "Terahertz sensor for non-contact thickness and quality measurement of automobile paints of varying complexity," *IEEE Trans Terahertz Sci Technol.*, vol. 4, no. 4, pp. 432-439, 2014.
- [18] S. Krimi, J. Klier, J. Jonuscheit, G. von Freymann, R. Urbansky, and R. Beigang, "Highly accurate thickness measurement of multi-layered automotive paints using terahertz technology," *Appl. Phys. Lett.*, vol. 109, no. 2, pp. 021105, 2016.
- [19] T. Chang, Q. Guo, L. Liu, and H.L. Cui, "Hilbert-transform-based accurate determination of ultrashort-time delays in terahertz time-domain spectroscopy," *IEEE Trans Terahertz Sci Technol.*, vol. 7, no. 5, pp. 514-520, 2017.
- [20] M. Zhai, A. Locquet, and D.S. Citrin, "Pulsed THz imaging for thickness characterization of plastic sheets," *NDT & E Int.*, vol. 116, pp. 102338, 2020.
- [21] B. Qiao, X. Zhang, J. Gao, R. Liu, and X. Chen, "Sparse deconvolution for the large-scale ill-posed inverse problem of impact force reconstruction," *Mech Syst Signal Process.*, vol. 83, pp. 93-115, 2017.
- [22] A. Beck, and M. Teboulle, "A fast iterative shrinkage-thresholding algorithm for linear inverse problems," *SIAM J Imaging Sci.*, vol. 2, no. 1, pp. 183-202, 2009.
- [23] I. Daubechies, M. Defrise, and C. De Mol, "An iterative thresholding algorithm for linear inverse problems with a sparsity constraint," *Commun. Pure Appl. Math.*, vol. 57, no. 11, pp. 1413-1457, 2004.
- [24] J.M. Bioucas-Dias, and M.A. Figueiredo, Two-step algorithms for linear inverse problems with non-quadratic regularization, in 2007 IEEE International Conference on Image Processing 2007 (Vol. 1, pp. I-105). IEEE.
- [25] J.M. Bioucas-Dias, and M.A. Figueiredo, "A new TwIST: Two-step iterative shrinkage/thresholding algorithms for image restoration," *IEEE Trans Image Process.*, vol. 16, no. 12, pp. 2992-3004, 2007.
- [26] X. Huang, K. He, S. Yoo, O. Cossairt, A. Katsaggelos, N. Ferrier, and M. Hereld, An Interior Point Method for Nonnegative Sparse Signal Reconstruction, In 2018 25th IEEE International Conference on Image Processing (ICIP) 2018 (pp. 1193-1197). IEEE.
- [27] K. Koh, S.J. Kim, and S. Boyd, "An interior-point method for large-scale l_1 -regularized logistic regression," *J Mach Learn Res.* vol. 8, pp. 1519-1555, 2007.
- [28] M. Naftaly, and R.E. Miles, "Terahertz time-domain spectroscopy for material characterization," *Proc. IEEE*, vol. 95, no. 8, pp. 1658-1665, 2007.
- [29] M.S. Islam, C.M.B. Cordeiro, M.J. Nine, J Sultana, A.L.S. Cruz, A. Dinovitsner, B.W. Ng, H. Ebendorff-heidepriem, D. Losic, and D. Abbott, "Experimental Study on Glass and Polymers: Determining the Optimal Material for Potential Use in Terahertz Technology," *IEEE Access*, vol. 8, 97204-97214, 2020.
- [30] D.M. Mittleman, R.H. Jacobsen, and M.C. Nuss, "T-ray imaging," *IEEE J Sel Top Quantum Electron.*, vol. 2, no. 3, pp. 679-692, 1996.
- [31] J. Pei, P. Ye, and W. Xie, Optimal wavelet analysis for THz-TDS pulse signals, In Photonics and Optoelectronics Meetings (POEM) 2008: Terahertz Science and Technology 2009 (Vol. 7277, p. 727708), International Society for Optics and Photonics.

- [32] M. Srivastava, C.L. Anderson, and J.H. Freed, "A new wavelet denoising method for selecting decomposition levels and noise thresholds," *IEEE Access*, vol. 4, pp. 3862-3877, 2016.
- [33] Y.S. Jin, G.J. Kin, and S.G. Jeon, "Terahertz dielectric properties of polymers," *J. Korean Phys. Soc.*, vol. 49, no. 2, pp. 513-517, 2006.
- [34] Y. Chang, Y. Zi, J. Zhao, Z. Yang, W. He, and H. Sun, "An adaptive sparse deconvolution method for distinguishing the overlapping echoes of ultrasonic guided waves for pipeline crack inspection," *Meas Sci Technol.*, vol. 28, no. 3, pp. 035002, 2017.
- [35] Y. Xu, X. Fang, S. Fan, L. Zhang, R. Yan, and X. Chen, "Double Gaussian mixture model-based terahertz wave dispersion compensation method using convex optimization technique," *Mech. Syst. Signal Process.*, vol. 164, pp. 108223, 2022.